

Journal Pre-proofs

Reversible lithium storage in sp^2 hydrocarbon frameworks

Zhangxiang Hao, Junrun Feng, Yiyun Liu, Liqun Kang, Bolun Wang, Junwen Gu, Lin Sheng, Ruoyu Xu, Sushila Marlow, Dan J.L. Brett, Yunhui Huang, Feng Ryan Wang

PII: S2095-4956(21)00409-5
DOI: <https://doi.org/10.1016/j.jechem.2021.07.019>
Reference: JECHEM 2066

To appear in: *Journal of Energy Chemistry*

Received Date: 26 February 2021
Revised Date: 22 July 2021
Accepted Date: 26 July 2021

Please cite this article as: Z. Hao, J. Feng, Y. Liu, L. Kang, B. Wang, J. Gu, L. Sheng, R. Xu, S. Marlow, D.J.L. Brett, Y. Huang, F.R. Wang, Reversible lithium storage in sp^2 hydrocarbon frameworks, *Journal of Energy Chemistry* (2021), doi: <https://doi.org/10.1016/j.jechem.2021.07.019>

This is a PDF file of an article that has undergone enhancements after acceptance, such as the addition of a cover page and metadata, and formatting for readability, but it is not yet the definitive version of record. This version will undergo additional copyediting, typesetting and review before it is published in its final form, but we are providing this version to give early visibility of the article. Please note that, during the production process, errors may be discovered which could affect the content, and all legal disclaimers that apply to the journal pertain.

© 2021 Published by ELSEVIER B.V. and Science Press on behalf of Science Press and Dalian Institute of Chemical Physics, Chinese Academy of Sciences.



Reversible lithium storage in sp^2 hydrocarbon frameworks

Zhangxiang Hao^{a,1}, Junrun Feng^{a,1}, Yiyun Liu^a, Liqun Kang^a, Bolun Wang^a, Junwen Gu^d, Lin Sheng^a, Ruoyu Xu^a, Sushila Marlow^a, Dan J.L. Brett^c, Yunhui Huang^{b,*},
Feng Ryan Wang^{a,*}

^a *Materials and Catalysis Laboratory, Department of Chemical Engineering, University College London, London WC1E 7JE, United Kingdom*

^b *School of Materials Science and Engineering, Huazhong University of Science and Technology, Wuhan 430074, Hubei, China*

^c *Electrochemical Innovation Lab, Department of Chemical Engineering, University College London, London, WC1E 7JE, United Kingdom*

^d *Department of Chemistry, University College London, London, WC1H 0AJ, United Kingdom*

***Corresponding authors.**

E-mail addresses: huangyh@hust.edu.cn (Y. Huang), ryan.wang@ucl.ac.uk (F.R. Wang)

1 These authors contributed equally to this work.

ABSTRACT

Polymer materials offer controllable structure-dependent performances in separation, catalysis and drug release. Their molecular structures can be precisely tailored to accept Li^+ for energy storage applications. Here the design of sp^2 carbon-based polyphenylene (PPH) with high lithium-ion uptakes and long-term stability is reported. Linear-PPH (L-PPH) exceeds the performance of crosslink-PPH (C-PPH), due to the fact that it has an ordered lamellar structure, promoting the Li^+ intercalation/deintercalation channel. The L-PPH cell shows a clear charge and discharge plateau at 0.35 and 0.15 V vs. Li^+/Li , respectively, which is absent in the C-PPH cell. The Li^+ storage capacity of L-PPH is five times that of the C-PPH. The reversible storage capacity is further improved to 261 mAh g^{-1} by functionalizing the L-PPH with the $-\text{SO}_3\text{H}$ groups. In addition, the Li-intercalated structures of C-PPH and L-PPH are investigated via near-edge X-ray absorption fine structure (NEXAFS), suggesting the high reversible Li^+ - C=C bond interaction at L-PPH. This strategy, based on new insight into sp^2 functional groups, is the first step toward a molecular understanding of the structure storage-capacity relationship in sp^2 carbon-based polymer.

Keywords: Lithium-ions battery; Organic anode; Topological structure; sp^2 hydrocarbon

1. Introduction

Lithium-ion batteries (LIBs) are a major innovation in the last century for energy storage [1–9], enabling the application of smart phones, electric vehicles and many other portable devices [6,10–12]. The mainstream of LIBs uses inorganic Li intercalation materials as anode to achieve an excellent cycling performance, such as

lithium transition metal oxides or phosphates and graphitic carbons [13–15]. Those electrode materials have issues of toxicity, high cost and involve considerable energy consumption during production [16–19]. In addition, the most common used graphitic carbon based anode shows stable hexatomic ring structure, which has little room of improvement due to its stable molecular structure [20–23]. This calls for materials innovations with flexible and controllable structure for high-capacity LIB systems.

Organic electrodes, especially polymers, are good alternatives for LIBs anodes [24]. Polymer materials provide precise molecular structures and controllable topological structures, leading to a structure-dependent performance in catalysis, separation, and drug release [25–29]. Their synthetic diversity and organic nature are also ideal for adsorption and redox reactions [6], enabling their application in energy storage systems. In recent years, different types of organic electrodes have been reported, including organic conjugated carbonyl compounds [30], organo-disulfides [31,32] and thioethers [33,34]. These materials are made from earth abundant elements and have high structure diversity, high flexibility and noteworthy electrochemical performance [11,35–37]. However, those organic electrode materials still face challenges, such as cycling performance and a relatively low potential difference between cathode and anode [10,11,38]. For example, thioethers show high solubility in organic electrolytes and a poor reaction efficiency for the S=O bond [39], leading to compromised cycling stability. The presence of oxygen and sulfur functional groups leads to relatively high discharge potentials (typically 0.5–2.0 V vs. Li^+/Li) [18,40,41], limiting their application as anodes. The design of organic anode materials with low redox potentials, high chemical stability and good cycling performance will then provide new materials-based solutions for the challenges in LIBs.

Within polymer anodes, the precise molecular control over their repeating unit enables the optimization of the local chemical environment, leading to high storage capacity. In comparison, the effect of topological structure, which can affect the Li^+ storage kinetics, is seldom reported in polymer anodes. Recently, Zhao et al. reported the design of three-dimensional networks mimicking the structure of diamond. It is built with sp - sp^3 hybridized polytetraethynylmethane, offering micro and mesopores that store Li-ions [42]. On one hand, it is suggested that highly cross-linked polymer shows a higher porosity and larger surface area, showing better potential when applied in electrodes [43]. On the other hand, the highly cross-linked polymer should have interspace and structure resistance leading to the high voltage platform in charge/discharge process [11,20,44]. To validate such understanding, it is important to compare the storage performance of polymer anodes with different topological structures but same or similar molecular structure.

In light of the topological structure of conventional carbon-based electrodes, in which sp^2 carbons are dominant, here polyphenylene (PPH) based Li anodes are designed with the controllable molecular and topological structures. The polymer consists of benzene groups, which can reversibly intercalate and de-intercalate a Li-ion to form a complex of Li/C_6 , behaving as ‘aromatic anodes’ [45,46]. The design includes a one-dimensional linear shape PPH (L-PPH) and a two-dimensional crosslink PPH (C-PPH) (Fig. 1a) that are based on identical repeating units (benzene groups $\text{C}_6\text{H}_{2/4}$). This strategy, based on new insight into sp^2 functional groups, is the first step toward a molecular understanding of the structure-storage capacity relationship. The PPH-based electrode achieved an extremely low discharge potential platform of 0.15 V vs. Li^+/Li , surpassing most reported polymer anodes in the literature [18,40,41]. The Li^+ storage capacity of L-PPH is five times that of the C-

PPH, due to the lamellar structure of L-PPH that promotes Li^+ transportation and storage. A reversible capacity of 194 mAh g^{-1} and cycle stability with only 0.25% capacity fade per cycle over 180 cycles were obtained by L-PPH-based electrodes under a current density of 50 mA g^{-1} . Furthermore, functionalization of L-PPH with $-\text{SO}_3\text{H}$ improves the reversible capacity to 261 mAh g^{-1} at current density of 50 mA g^{-1} . In addition to long-term performance, outstanding cycle stability, with only 0.14% capacity fade per cycle for 500 cycles under a higher current density of 100 mA g^{-1} , was achieved. Near-edge X-ray absorption fine structure (NEXAFS) was performed to investigate Li-intercalated structures of C-PPH and L-PPH based electrodes.

2. Experimental

2.1. Synthesis of PPH-based material

Crosslink PPH (C-PPH): To obtain a fully crosslinked PPH polymer framework, 1,2,4,5-tetrabromobenzene (1.531 g, 3.89 mmol) and benzene-1,4-diboronic acid (1.289 g, 7.78 mmol) were added into 120 mL dimethylformamide. The mixture was degassed through three freeze-pump-thaw cycles. K_2CO_3 (2.0 mol L^{-1} , 15 mL) and $\text{Pd}(\text{PPh}_3)_4$ (0.3 g, 0.25 mmol) were introduced with three subsequent freeze-pump-thaw cycles. The mixture was then purged with Ar and heated to $150 \text{ }^\circ\text{C}$ for 20 h while stirring. The product precipitated, and then was washed with water, dichloromethane and methanol. Polymers were treated with $\text{HCl}/\text{H}_2\text{O}_2$ (5:1, v/v) solution to remove palladium (Pd) residue from the cross-coupling reaction. The mixture was stirred overnight at room temperature and subsequently heated to $60 \text{ }^\circ\text{C}$ for 2 h. The product was then washed with water and methanol. Approximately 600 mg of grey product was obtained in per batch. Linear PPH (L-PPH): L-PPH was

obtained by combining Benzene-1,4-diboronic acid with 1,4-dibromobenzene in a ratio of 1:1.

2.2. Synthesis of L-PPH-SO₃H material

After drying in a vacuum oven overnight, 200 mg of the H₂O₂ treated polymer was mixed with 5 mL concentrated sulfuric acid (98 wt%), stirring at 40 °C for 16 h. Above product was poured into 200 mL deionized water and filtered, before washing with H₂O and methanol until neutral pH to eliminate physically absorbed sulfuric acid molecules within the pores. Obtained L-PPH-SO₃H catalysts were dried in vacuum oven at 50 °C overnight. The L-PPH-SO₃H-No treatment was fabricated without the HCl/H₂O₂ treatment and other steps are all the same.

2.3. Electrochemical measurements

All the electrochemical measurements were performed with 2032 coin cells using Li foil as anode. 1 mol L⁻¹ LiPF₆ in an ethylene carbonate (EC) and diethylene carbonate (DEC) (3:7, v/v) solution with fluoroethylene carbonate (FC) (2 wt%) was used as the electrolyte and the ratio of active materials to electrolyte was maintained at 1:10 for all cells. The PPH electrode was prepared by mixing PPH, super P, graphene, carboxymethyl cellulose (CMC) and styrene-butadiene rubber (SBR) in a weight ratio of 70:15:5:5:5 in deionized water. The slurry was coated on Cu foil and dried at 80 °C overnight in an oven. Finally, the electrode was punched into round discs with a diameter of 6 mm. The mass loading at the cathode ranged from 1–2 mg cm⁻². Cyclic voltammetry (CV) measurements were conducted on an electrochemical workstation (Gamry) at a scan rate of 0.05 mV s⁻¹ with a cut off voltage range of 0.1–1.5 V vs. Li⁺/Li at room temperature. Galvanostatic charge and discharge were tested within a voltage window of 0.1–1.5 V vs. Li⁺/Li on a battery measurement system (Neware, China).

2.4. Characterization

Bright field (BF) and high angle annular dark field-scanning transmission electron microscopy (HAADF-STEM) images were acquired on probe-corrected (CEOS) scanning transmission electron microscope (JEM ARM 200CF, JEOL, Japan) with an acceleration voltage of 200 kV. Energy-dispersive X-ray spectroscopy (EDS) and elemental mapping data were obtained on the same microscope. The Brunauer-Emmett-Teller (BET) surface area was calculated according to the adsorption data in the relative pressure range from 0.06 to 0.2. Thermogravimetric analysis (TGA) was measured on PerkinElmer Pyris 1 TGA. 2–10 mg sample is heated from 30 to 700 °C with a heating rate of 10 °C min⁻¹. Attenuated total reflection infrared (ATR-IR) spectroscopy is measured with Bruker ALPHA FTIR spectrometer. Small angle X-ray scattering (SAXS) signal were detected by using the SAXSLAB GANESHA which collimation was motorized slits with single crystal blades and the Q range varied from 0.0025 to 3 Å⁻¹. A Cu-K_α radiation was used for powder X-ray diffraction (PXRD), with a wavelength of 1.54 Å. The distance from the detector varied from 80 to 1450 nm. One of four scattering mode can be chosen, which are extremely small angle SAXS (ESAXS), SAXS, medium angle SAXS (MAXS) and wild angle SAXS (WAXS). The samples were analysed in 0.15 mm capillary under vacuum. NEXAFS was performed at the beamline B07-C at the diamond light source. Spectra were recorded at the C K-edge at 280–295 eV in total electron yield (TEY) mode. PPH based electrode samples were prepared by mixing with PPH based material, conductive materials and binder as described above. The sample was fully discharged first and then taken out from the cell in the glovebox. With the protection by argon, sample was transferred from lab to beam line, installed in the preparation chamber and then inserted into the experimental chamber in 3 min. Charged samples were

prepared in the same way.

3. Results and discussion

PPH is synthesized via the palladium-catalyzed Suzuki cross-coupling reaction of 1,2,4,5-tetrabromobenzene, 1,4-dibromobenzene and benzene-1,4-diboronic acid as shown in experimental section. L-PPH is obtained with the pure di-substituted benzene group ($C_6H_4^-$), while the cross-link structure of the C-PPH originates from the partial replacement of the $C_6H_4^-$ with tetra-substituted benzene group ($C_6H_2^-$) (Fig. 1a). Thus, L-PPH and C-PPH have similar repeating units but different topological structures. Such a difference will be reflected in the macroscopic properties, which determine Li^+ storage performance.

The similar repeating units in the L-PPH and C-PPH lead to similar chemical environments at the molecular level. This is verified in both infrared and solid-state ^{13}C nuclear magnetic resonance (NMR) spectroscopy. There is no major difference in the IR spectra between L-PPH and C-PPH (Fig. 1b). The absorption bands at around 3028 cm^{-1} in both spectra represent the aromatic C–H stretch. The aromatic C=C bonds are found at 810 cm^{-1} . The solid-state ^{13}C NMR spectrum of L-PPH shows two sharp peaks at 136.4 and 125.6 ppm in the characteristic region of sp^2 carbon atoms, which correspond to the connecting (136.4 ppm) and non-connecting (125.6 ppm) carbon atoms in the substituted benzene groups (Fig. 1c, black). The peak positions shift towards higher ppm values by 3–4 ppm in the C-PPH (Fig. 1c, red), due to the presence of more aryl substitution groups that promote the electron-withdrawing effect to the sp^2 carbons. The C-PPH peaks are broader than those in the L-PPH spectra, indicating that the carbon chemical environment of carbon is less defined.

The IR and solid-state ^{13}C NMR spectra show a similar molecular structure for the L-PPH and C-PPH, with little variation. On the other hand, their macroscopic structures, in terms of morphology and porosity, are different due to their original topological structures (linear vs. crosslink). At the nm scale, both L-PPH and C-PPH are amorphous. The C-PPH is in the form of small particles with sizes in the range of 50–200 nm that are aggregating together (Fig. 2d). In comparison, the presence of small and individual particles is not obvious for L-PPH (Fig. 2a). At the μm scale, the overall structure in L-PPH is more integrated throughout the whole particle in the form of a lamellar structure (Fig. 2b), whereas C-PPH is less integrated, showing the particle feature (Fig. 2e). This is also visible in the HAADF-STEM images, showing a more homogeneous distribution in L-PPH than that in C-PPH (Fig. 2c and f). The SAXS pattern (Fig. 2g) shows no obvious scattering feature for C-PPH. L-PPH has a small peak at $Q = 0.276 \text{ nm}^{-1}$, suggesting a high ordering of lamellar structure with an intersheet spacing of $d = 23 \text{ nm}$. Such short-range layer by layer structures is common in linear shape polymers [47–49]. The linear chains pack into films, contributing to a non-porous structure with a very low N_2 uptake and a BET surface area of only $41 \text{ m}^2 \text{ g}^{-1}$ (Fig. 2h). In comparison, crosslink polymers can form intrinsic micropores according to their structure [50]. The similar behaviour is observed for C-PPH, showing up to $200 \text{ cm}^3 \text{ g}^{-1}$ of N_2 adsorption at P/P_0 below 0.1 (Type I N_2 adsorption isotherm). A BET surface area of $652 \text{ m}^2 \text{ g}^{-1}$ is calculated (Fig. 2h), suggesting the effectiveness of the cross-linking that forms micropores, as indicated in Fig. 1(a).

The results above show the C-PPH and L-PPH have similar repeating molecular units but different topological structures. Thus, the structure dependent Li^+ storage performance can be studied for a porous material (C-PPH) and a non-porous material with lamellar structure (L-PPH). To achieve this, PPH-based electrodes were

assembled with Li metal electrodes in coin cells. The electrolyte used is 1 mol L⁻¹ LiPF₆ in an EC and DEC (3:7, v/v) solution with FC (2 wt%) and the ratio of active materials to electrolyte was maintained at 1:10 for all cells. The coin cells run at a current density of 50 mA g⁻¹. For the first discharge, the specific capacity of C-PPH is around 340 mAh g⁻¹, and the reversible specific capacity is less than 40 mAh g⁻¹ (Fig. 3a), which is much lower than that of L-PPH at 194 mAh g⁻¹ (Fig. 3b). The higher reversible storage capacity of L-PPH suggests a high density of active sites compared to that of the C-PPH. The reversible specific capacity corresponds to one Li⁺ per two substituted benzene groups (ESI calculations). Based on the charge and discharge curve of the 2nd cycle, both charge and discharge plateau are observed for L-PPH whereas the C-PPH cell is not obvious. The charge and discharge curve for the 2nd and 5th cycle overlap the L-PPH cell, whereas the reversibility of the C-PPH is low. A comparison of 10th, 30th and 50th cycles (Fig. S1) show a higher reversible capacity of L-PPH than that of C-PPH, and L-PPH still has a clear charge/discharge plateau after 50 cycles. The CV curves measured at a scan rate of 0.05 mV s⁻¹ with a voltage window of 0.1 to 1.5 V vs. Li⁺/Li, which is the desired for testing anode materials. The cell with L-PPH electrode shows the cathodic peak at ~0.10 V, corresponding to the Li⁺ intercalation. The subsequent anodic peak at ~0.35 V is related to the Li⁺ de-intercalation (Fig. 3c black). In comparison, the anodic peak for the C-PPH cell is not obvious, indicating that the Li⁺ de-intercalation is not efficient. This also explains the low reversible storage capacity of the C-PPH cell. The cathodic and anodic peak position correspond well with the discharge and charge plateaus located at ~0.15 and ~0.35 V, respectively. The very low value of the discharge plateau offers high working potentials for LIBs, which is seldom reported in the literature [18,40,41]. The rate performance of the L-PPH cell shows reversible capacity of 242, 183, 154, 131,

113, 99, 88, 79 and 71 mAh g⁻¹ at 25, 50, 100, 150, 200, 250, 300, 350 and 400 mA g⁻¹, respectively. When the rate is reset back to 50 mAh g⁻¹ after running at various rates, a reversible capacity of 163 mAh g⁻¹ is recovered, corresponding to a capacity retention of 89% (Fig. 3d). In comparison, the rate performance of the C-PPH cell is much lower, at 135, 65, 50, 42, 37, 33, 30, 28 and 27 mAh g⁻¹ for the corresponding current densities shown above.

In the long-term cycle performances (Fig. 3e), the L-PPH cell achieves a reversible capacity of 194 mAh g⁻¹ and maintains 116 mAh g⁻¹ after 180 cycles, delivering a capacity fade of only 0.25% per cycle. In contrast, the C-PPH cell shows a reversible capacity of only 39 mAh g⁻¹. The origin of the superior performance of the L-PPH cell comes from its lamellar structure at the macroscopic scale, enabling access of 54% of the substituted benzene groups. The stark difference between L-PPH and C-PPH is possibly due to the trapping of Li⁺ at the entrance of the micropores, blocking the further Li⁺ intercalation [51,52]. Corresponding to the electrochemical performance, NEXAFS of C K-edge was performed to study the change of carbon structure before and after Li⁺ intercalation. Four major peaks are observed on both C-PPH (Fig. 3f) and L-PPH (Fig. 3g): 284 eV for C=C bond; 287 and 288.3 eV for C-H bond and 292 eV for C-C bond. C-PPH shows a stable C=C bond regardless of Li⁺ intercalation and deintercalation. In contrast, Li-ion intercalation significantly reduced the C=C peaks at L-PPH sample, whereas it is recovered after Li-ion deintercalation (Fig. 3g). We hypothesize that this is due to the interaction between C=C bond with Li⁺ in the framework. The result suggests that the C=C bond at L-PPH has much higher interaction with Li⁺ than that at C-PPH. After charging, the C=C bond shows a good recovery, consistent with high reversible capacity of L-PPH electrodes.

Considering the good cycling performance of the L-PPH cell, the $-\text{SO}_3\text{H}$ group is functionalized onto the L-PPH to further boost the storage capacity. The $-\text{SO}_3\text{H}$ group is reported to bring more active sites and improve electrochemical cycling stability by enhancing ionic conductivity and Li^+ diffusion efficiency [53–56]. The successful loading of $-\text{SO}_3\text{H}$ sites is confirmed by the new IR vibrational modes at 1032 and 1100 cm^{-1} , corresponding to the S=O stretching. (Fig. S2). After the reaction, a density of 0.48 mmol g^{-1} of the $-\text{SO}_3\text{H}$ group is obtained in the material, which does not change the lamellar morphology and porosity (Fig. 4a and b, Figs S3 and S4). The N_2 -physisorption isotherms is similar to the L-PPH's (Fig. S3), showing the no porous nature. Meanwhile, the loading of the $-\text{SO}_3\text{H}$ is uniform, as shown in the EDS map of carbon and sulfur (Fig. 4c). The solid-state NMR spectrum of L-PPH- SO_3H reveals very little change from that of L-PPH (Figs 4d and 1c). TG curve of L-PPH- SO_3 suggests the composite is stable up to 350 $^\circ\text{C}$ (Fig. S5). The CV curve shows the functionalization does not change the position of anodic and cathodic peaks compared to the L-PPH (Figs 4e and 3c). The $-\text{SO}_3\text{H}$ group improves the rate performance, especially at low current density (25 and 50 mA g^{-1}) (Fig. 4f). The cycling performance exhibits a high reversible capacity of 261 mAh g^{-1} and retained a capacity of 186 mAh g^{-1} after 180 cycles (Figs S6 and S7), which are 67 and 70 mAh g^{-1} higher than those of L-PPH. The reversible capacity of C-PPH is lower than 50 mAh g^{-1} . The improvement corresponds to the intercalation of five additional Li^+ per SO_3H group. Such an increase of Li storage has also been reported in other similar systems for polymer electrodes [45,54,57,58]. In addition to long cycle stability, a capacity of 104 mAh g^{-1} was sustained after 500 charge/discharge cycles at a high current density of 100 mA g^{-1} , with a low-capacity fade rate of 0.14% per cycle (Fig. 4g). We synthesized L-PPH- SO_3H without $\text{H}_2\text{O}_2/\text{HCl}$ treatment. The cell with L-PPH-

SO₃H (No treatment) electrode shows similar CV with L-PPH-SO₃H (Fig. S8a), revealing the same reaction process and Li⁺ storage mechanism. The cycling performances of both cells are also very similar (Fig. S8b). We conclude that the H₂O₂/HCl treatment does not affect the performance of L-PPH-SO₃H. NEXAFS of fresh and discharged electrodes shows the decrease of C=C peak at 284.5 eV (Fig. 4h). In addition, L-PPH-SO₃H electrode shows a relatively lower C=C peak than that of L-PPH after discharging, suggesting a higher degree of Li⁺ intercalation in the SO₃H functionalized electrode (Fig. S9). Therefore, the SO₃H group changes the Li-ion storage ability of the whole carbon framework and contributes to more Li-ions intercalation.

4. Conclusions

*sp*² dominant carbon-based polymer electrodes were designed to store lithium ions. The design includes a one-dimensional linear shape PPH and a two-dimensional crosslink PPH. The different macroscopic structure, but the similar chemical environment, enables us to study the effect of topological structure on lithium uptake ability. The designed PPH electrode shows a very low discharge plateau of 0.15 V vs. Li⁺/Li, surpassing the most reported values for polymer anode in the literature [18,40,41]. The lithium storage performance was achieved in L-PPH, with a reversible capacity of 194 mAh g⁻¹ at 50 mA g⁻¹ rate, which is five-times the capacity of C-PPH. Furthermore, L-PPH also shows better high-rate performance and cycling stability. With a similar molecular structure, the electrochemical results suggest the Li⁺ storage capacity can be varied a lot by changing the topological packing of the materials. Micropores are not always better than nonporous materials. Considering the complexity of polymer systems, the conclusions we drawn from our PPH system is challenging to extend to other polymer system. However, it has certain indications as

the most polymer-based anodes use sp^2 carbon as the major active sites [10,22–24,43,44,59–67]. Functionalization of the $-SO_3H$ group further boosts the reversible capacity to 261 mAh g^{-1} at 50 mA g^{-1} rate. With a current density of 100 mA g^{-1} , a good cycle stability with only 0.14% capacity fade per cycle for over 500 cycles is achieved. NEXAFS was performed on C-PPH and L-PPH based electrodes. It shows a different Li-intercalated carbon structure between two polymers.

Acknowledgement

The project is funded by the Engineering and Physical Sciences Research Council (EPSRC) (EP/P02467X/1 and EP/S018204/1) and the Centre for Nature Inspired Chemical Engineering (EP K038656/1). We acknowledge Diamond Light Source for the session (EM22572, MG21641, MG22604) for STEM and TEM measurements while SI26717, SI29407 for NEXAFS measurements on C K -edge.

References

- [1] Q. Pang, X. Liang, C.Y. Kwok, L.F. Nazar, Nat. Energy. 1 (2016) 1–11.
- [2] Y. Sun, N. Liu, Y. Cui, Nat. Energy 1 (2016) 1-12
- [3] Z. Hao, L. Yuan, Z. Li, J. Liu, J. Xiang, C. Wu, R. Zeng, Y. Huang, Acta. 200 (2016) 197–203.
- [4] L.M. Zhu, A.W. Lei, Y.L. Cao, X.P. Ai, H.X. Yang, Chem. Commun. 49 (2013) 567–569.
- [5] C. Li, X. Hu, X. Lou, Q. Chen, B. Hu, Chem. Commun. 52 (2016) 2035–2038.
- [6] J. Du, Y. Li, H. Liu, W. Shi, L. V. Moskaleva, P. Cheng, ACS Appl. Mater. Interfaces. 11 (2019) 25863–25869.
- [7] Z. Zhu, A. Kushima, Z. Yin, L. Qi, K. Amine, J. Lu, J. Li, Nat. Energy 1 (2016) 1–7.
- [8] C. Chen, Y. Wen, X. Hu, X. Ji, M. Yan, L. Mai, P. Hu, B. Shan, Y. Huang, Nat. Commun. 6 (2015) 1–8.
- [9] Z. Jian, W. Han, X. Lu, H. Yang, Y.S. Hu, J. Zhou, Z. Zhou, J. Li, W. Chen, D. Chen, L. Chen, Adv. Energy Mater. 3 (2013) 156–160.
- [10] W. Wei, G. Chang, Y. Xu, L. Yang, J. Mater. Chem. A. 6 (2018) 18794–18798.
- [11] J. Wu, X. Rui, C. Wang, W.B. Pei, R. Lau, Q. Yan, Q. Zhang, Adv. Energy Mater. 5 (2015) 1-6
- [12] P.G. Bruce, S.A. Freunberger, L.J. Hardwick, J.-M. Tarascon, Nat. Mater. 11 (2012) 19–29.
- [13] G.N. Zhu, H.J. Liu, J.H. Zhuang, C.X. Wang, Y.G. Wang, Y.Y. Xia, Energy Environ. Sci. 4 (2011) 4016–4022.
- [14] M.N. Obrovac, V.L. Chevrier, Chem. Rev. 114 (2014) 11444–11502.
- [15] H. Bin Wu, J.S. Chen, H.H. Hng, X.W. Lou, Nanoscale. 4 (2012) 2526–2542.
- [16] P. Poizot, F. Dolhem, Energy Environ. Sci. 4 (2011) 2003–2019.

- [17] Y. Liang, P. Zhang, S. Yang, Z. Tao, J. Chen, *Adv. Energy Mater.* 3 (2013) 600–605.
- [18] Y. Liang, Z. Tao, J. Chen, *Adv. Energy Mater.* 2 (2012) 742–769.
- [19] Y. Mao, Q. Kong, B. Guo, X. Fang, X. Guo, L. Shen, M. Armand, Z. Wang, L. Chen, *Energy Environ. Sci.* 4 (2011) 3442–3447.
- [20] Y. Lu, J. Chen, *Nat. Rev. Chem.* 4 (2020) 127–142.
- [21] X. Cao, J. Liu, L. Zhu, L. Xie, *Energy Technol.* 7 (2019) 1–24.
- [22] D. Mukherjee, G.Y.K. Gowda, H.M.N. Kotresh, S. Sampath, Porous, *ACS Appl. Mater. Interfaces.* 9 (2017) 19446–19454.
- [23] J. Wu, X. Rui, G. Long, W. Chen, Q. Yan, Q. Zhang, *Angew. Chemie - Int. Ed.* 54 (2015) 7354–7358.
- [24] G. Li, B. Zhang, J. Wang, H. Zhao, W. Ma, L. Xu, W. Zhang, K. Zhou, Y. Du, G. He, *Angew. Chemie - Int. Ed.* 58 (2019) 8468–8473.
- [25] F. Wang, J. Mielby, F.H. Richter, G. Wang, G. Prieto, T. Kasama, C. Weidenthaler, H.J. Bongard, S. Kegnaes, A. Fürstner, F. Schüth, *Angew. Chemie - Int. Ed.* 53 (2014) 8645–8648.
- [26] J. Lu, P.H. Toy, *Chem. Rev.* 109 (2009) 815–838.
- [27] T. Rodenas, I. Luz, G. Prieto, B. Seoane, H. Miro, A. Corma, F. Kapteijn, F.X. Llabrés I Xamena, J. Gascon, *Nat. Mater.* 14 (2015) 48–55.
- [28] M.R. Abidian, D.H. Kim, D.C. Martin, *Adv. Mater.* 18 (2006) 405–409.
- [29] S. Kramer, N.R. Bennedsen, S. Kegnaes, *ACS Catal.* 8 (2018) 6961–6982.
- [30] A.J. Wain, G.G. Wildgoose, C.G.R. Heald, L. Jiang, T.G.J. Jones, R.G. Compton, *J. Phys. Chem. B.* 109 (2005) 3971–3978.
- [31] N. Oyama, T. Tatsuma, T. Sato, T. Sotomura, *Nature* (1995) 598–600
- [32] N. Oyama, J.M. Pope, T. Sotomura, *J. Electrochem. Soc.* 144 (1997) L47–L51.
- [33] L. Zhan, Z. Song, N. Shan, J. Zhang, J. Tang, H. Zhan, Y. Zhou, Z. Li, C. Zhan, *J. Power Sources* 193 (2009) 859–863.
- [34] L. Zhan, Z. Song, J. Zhang, J. Tang, H. Zhan, Y. Zhou, C. Zhan, *Electrochim. Acta.* 53 (2008) 8319–8323.
- [35] S. Wang, L. Wang, Z. Zhu, Z. Hu, Q. Zhao, J. Chen, *Angew. Chemie - Int. Ed.* 53 (2014) 5892–5896.
- [36] W. Huang, Z. Zhu, L. Wang, S. Wang, H. Li, Z. Tao, J. Shi, L. Guan, J. Chen, *Angew. Chemie - Int. Ed.* 52 (2013) 9162–9166.
- [37] H. Yang, S. Zhang, L. Han, Z. Zhang, Z. Xue, J. Gao, Y. Li, C. Huang, Y. Yi, H. Liu, Y. Li, *ACS Appl. Mater. Interfaces* 8 (2016) 5366–5375.
- [38] L. Wang, X. He, W. Sun, J. Li, J. Gao, G. Tian, J. Wang, S. Fan, *RSC Adv.* 3 (2013) 3227–3231.
- [39] Z. Song, H. Zhou, *Energy Environ. Sci.* 6 (2013) 2280–2301.
- [40] M. Armand, S. Grugeon, H. Vezin, S. Laruelle, P. Ribière, P. Poizot, J.M. Tarascon, *Nat. Mater.* 8 (2009) 120–125.
- [41] W. Walker, S. Grugeon, H. Vezin, S. Laruelle, M. Armand, F. Wudl, J.M. Tarascon, *J. Mater. Chem.* 21 (2011) 1615–1620.
- [42] Z. Zhao, S. Das, G. Xing, P. Fayon, P. Heasman, M. Jay, S. Bailey, C. Lambert, H. Yamada, T. Wakihara, A. Trewin, T. Ben, S. Qiu, V. Valtchev, *Angew. Chemie - Int. Ed.* 57 (2018) 11952–11956.
- [43] W. Ma, C. Zhang, X. Gao, C. Shu, C. Yan, F. Wang, Y. Chen, J.H. Zeng, J.X. Jiang, *J. Power Sources* 453 (2020) 227868.
- [44] C. Luo, X. Ji, S. Hou, N. Eidson, X. Fan, Y. Liang, T. Deng, J. Jiang, C. Wang, *Adv. Mater.* 30 (2018) 1–9.

- [45] X. Han, G. Qing, J. Sun, T. Sun, *Angew. Chemie - Int. Ed.* 51 (2012) 5147–5151.
- [46] K. Sato, M. Noguchi, A. Demachi, N. Oki, M. Endo, *Science* (80-.). 264 (1994) 556–558.
- [47] M. Kumar, S. Kumar, *RSC Adv.* 5 (2015) 14871–14878.
- [48] H. Schlaad, H. Kukula, B. Smarsly, M. Antonietti, T. Pakula, *Polymer (Guildf)*. 43 (2002) 5321–5328.
- [49] J. Li, A. Jiao, S. Chen, Z. Wu, E. Xu, Z. Jin, *J. Mol. Struct.* 1165 (2018) 391–400.
- [50] J. Schmidt, J. Weber, J.D. Epping, M. Antonietti, A. Thomas, *Adv. Mater.* 21 (2009) 702–705.
- [51] M. Ghiyasiyan-Arani, M. Salavati-Niasari, *Compos. Part B Eng.* 183 (2020) 107734.
- [52] D. Aurbach, M.D. Levi, G. Salitra, N. Levy, E. Pollak, J. Muthu, *J. Electrochem. Soc.* 155 (2008) A745.
- [53] H. Hou, F. Vacandio, M.L. Di Vona, P. Knauth, *Acta.* 81 (2012) 58–63.
- [54] J. Duan, H. Hou, X. Liu, Q. Liao, S. Liu, Y. Yao, *Ionics (Kiel)*. 23 (2017) 3037–3044.
- [55] Y.J. Kim, H.J. Lee, S.W. Lee, B.W. Cho, C.R. Park, *Carbon N. Y.* 43 (2005) 163–169.
- [56] Y. Yang, F. Zheng, G. Xia, Z. Lun, Q. Chen, *J. Mater. Chem. A.* 3 (2015) 18657–18666.
- [57] D. Qin, L. Xue, B. Du, J. Wang, F. Nie, L. Wen, *J. Mater. Chem. A.* 3 (2015) 10928–10934.
- [58] Z. Wei, L. Xue, F. Nie, J. Sheng, Q. Shi, X. Zhao, *J. Power Sources* 256 (2014) 28–31.
- [59] H.G. Wang, S. Yuan, D.L. Ma, X.L. Huang, F.L. Meng, X.B. Zhang, *Adv. Energy Mater.* 4 (2014) 1–7.
- [60] J. Xie, X. Rui, P. Gu, J. Wu, Z.J. Xu, Q. Yan, Q. Zhang, *ACS Appl. Mater. Interfaces* 8 (2016) 16932–16938.
- [61] J. Xie, Z. Wang, P. Gu, Y. Zhao, Z.J. Xu, Q. Zhang, *Sci. China Mater.* 59 (2016) 6–11.
- [62] T. Sun, Z.J. Li, H.G. Wang, D. Bao, F.L. Meng, X.B. Zhang, *Angew. Chemie - Int. Ed.* 55 (2016) 10662–10666.
- [63] Z. Song, Y. Qian, M.L. Gordin, D. Tang, T. Xu, M. Otani, H. Zhan, H. Zhou, D. Wang, *Angew. Chemie - Int. Ed.* 54 (2015) 13947–13951.
- [64] Z. Li, W. Zhong, A. Cheng, Z. Li, L. Li, H. Zhang, *Electrochim. Acta.* 281 (2018) 162–169.
- [65] C. Zhang, Y. He, P. Mu, X. Wang, Q. He, Y. Chen, J. Zeng, F. Wang, Y. Xu, J.X. Jiang, *Adv. Funct. Mater.* 28 (2018).
- [66] L. Yang, W. Wei, Y. Ma, Y. Xu, G. Chang, *J. Power Sources* 449 (2020) 227551.
- [67] Y. Sun, Y. Sun, Q. Pan, G. Li, B. Han, D. Zeng, Y. Zhang, H. Cheng, *Chem. Commun.* 52 (2016) 3000–3002.

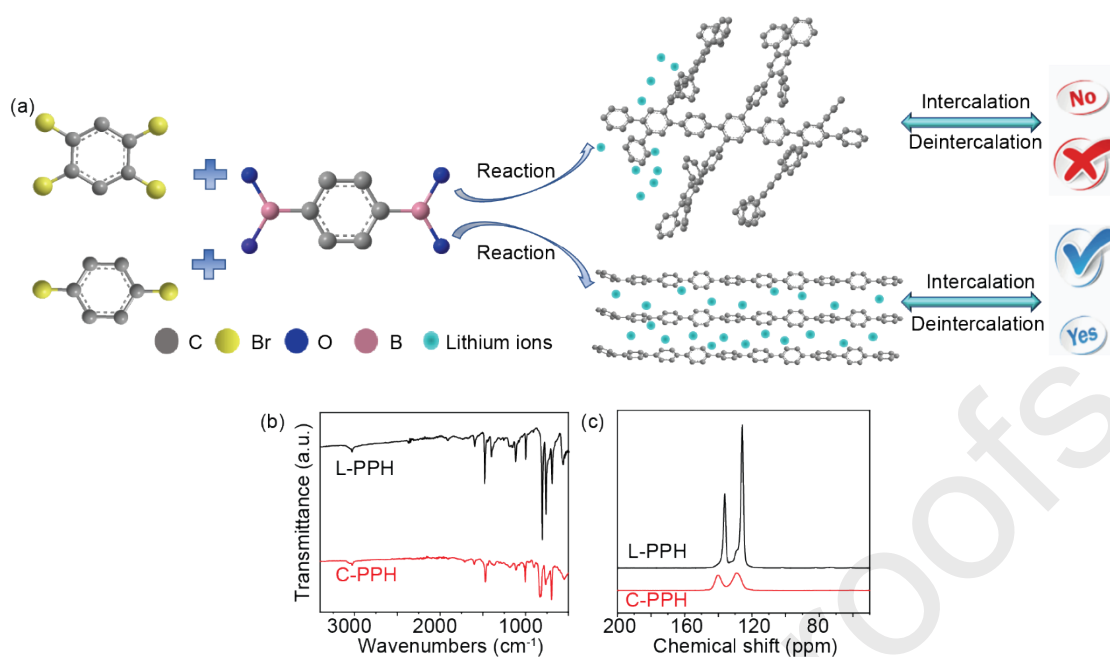


Fig. 1. (a) Fabrication process and schematic illustration of L-PPH and C-PPH. (b) ATR-IR spectroscopy of L-PPH and C-PPH. (c) solid-state ^{13}C NMR spectroscopy of L-PPH and C-PPH.

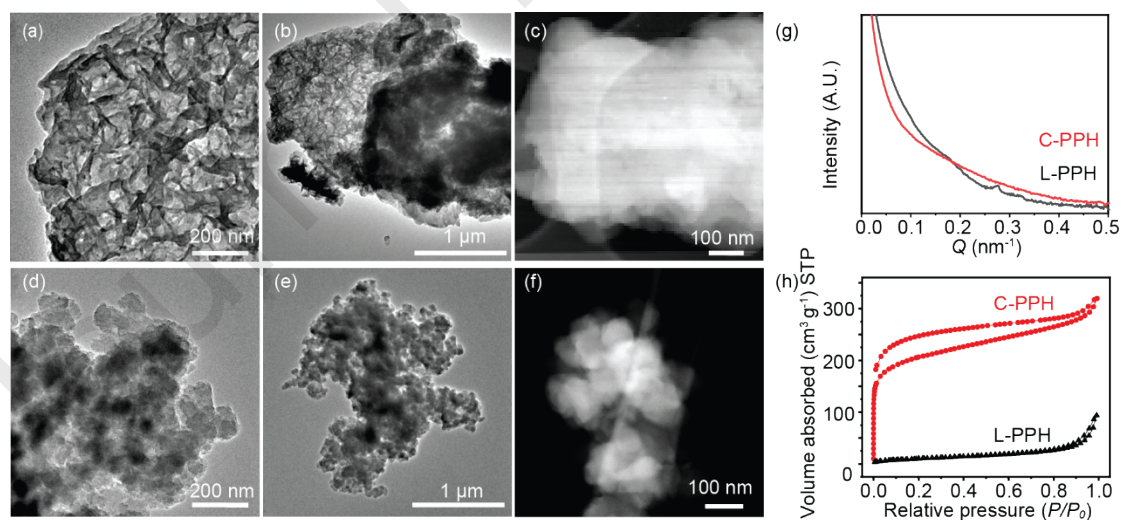


Fig. 2. TEM images of (a–c) L-PPH, and (d–f) C-PPH at different magnifications, (g) SAXS of L-PPH and C-PPH. (h) N_2 physisorption of L-PPH and C-PPH.

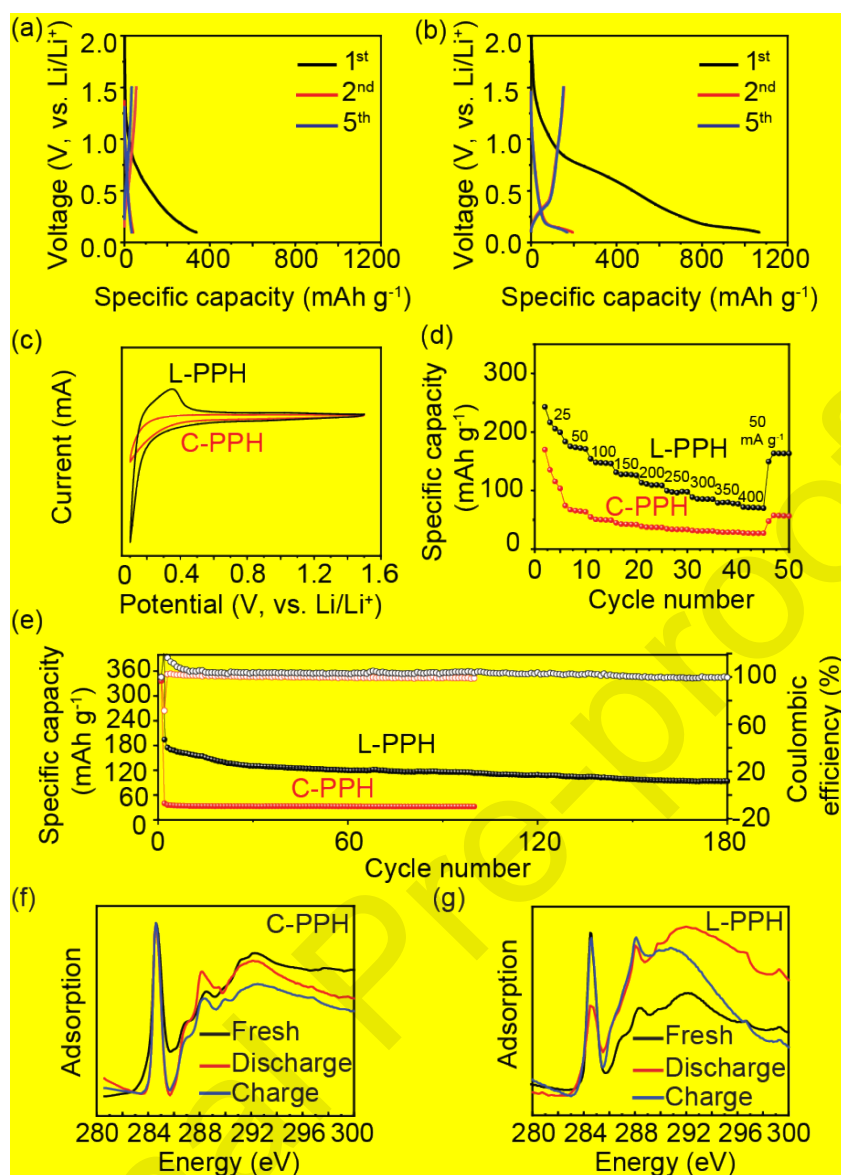


Fig. 3. Charge and discharge profiles of cells for (a) C-PPH electrode, (b) L-PPH electrode, (c) CV curves of the cell with L-PPH and C-PPH electrode between 0.1 and 1.5 V vs. Li^+/Li , (d) Rate performance of cell at a current rate ranging from 25 mA g^{-1} , (e) Long-term cycling of cell at a current density of 50 mA g^{-1} . **C K-edge NEXAFS of (f) C-PPH, (g) L-PPH, where Fresh is fresh polymer-based electrode, discharge is polymer-based electrode with fully discharged states and charge is polymer-based electrode with fully charged states.**

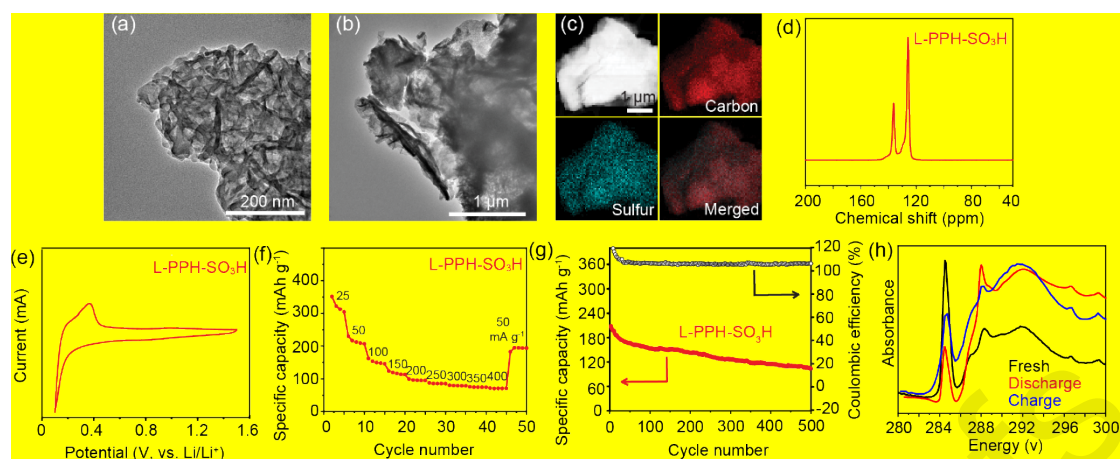
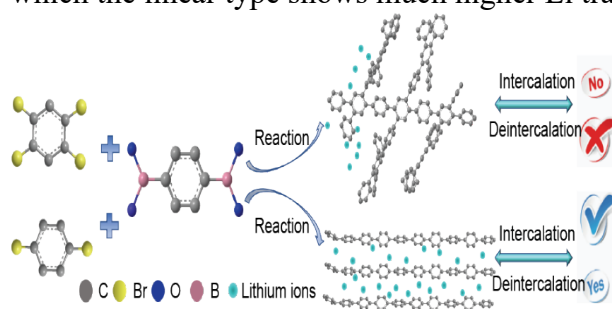


Fig. 4. (a, b) TEM images of L-PPH-SO₃H, (c) HAADF-STEM image and element C (red), S (cyan) and merged map, (d) Solid-state ¹³C NMR spectrum of L-PPH-SO₃H, (e) Charge and discharge profiles of the L-PPH-SO₃H cell, (f) Rate performance of cell at a current rate ranging from 25 to 400 mA g⁻¹, (g) Cycling performance and corresponding Coulombic efficiency of L-PPH-SO₃H at a current density of 100 mA g⁻¹ for 500 cycles, (h) NEXAFS of Fresh L-PPH-SO₃H electrode, fully discharge and fully charge L-PPH-SO₃H electrode.

Graphical Abstract

The linear and crosslink types of PPH provide different topological structures, in which the linear type shows much higher Li transfer and storage.



Electronic Supplementary Information (ESI) for**Reversible lithium storage in sp² hydrocarbon frameworks**

Zhangxiang Hao,^[a] ‡ Junrun Feng,^[a] ‡ Yiyun Liu,^[a] Liqun Kang,^[a] Bolun Wang,^[a]
Junwen Gu,^[d] Lin Sheng,^[a] Ruoyu Xu,^[a] Sushila Marlow,^[a] Dan J.L. Brett,^[c] Yunhui
Huang,^{*[b]} Feng Ryan Wang^{*[a]}

^a Materials and Catalysis Laboratory, Department of Chemical Engineering,
University College London, London WC1E 7JE, United Kingdom.
E-mail: ryan.wang@ucl.ac.uk (F. R. Wang).

^b School of Materials Science and Engineering, Huazhong University of Science and
Technology, Wuhan, Hubei 430074, China.
E-mail: huangyh@hust.edu.cn (Y.H. Huang).

^c Electrochemical Innovation Lab, Department of Chemical Engineering, University
College London, London, WC1E 7JE, United Kingdom.

^d Department of Chemistry, University College London, London, WC1H 0AJ, United
Kingdom.

‡ These authors contributed equally to this work

CONTENTS :

SUPPORTING FIGURES: FIGURE. S1-S9

CALCULATION OF PPH THEORETICAL STORAGE CAPACITY.

1. Supporting Figures

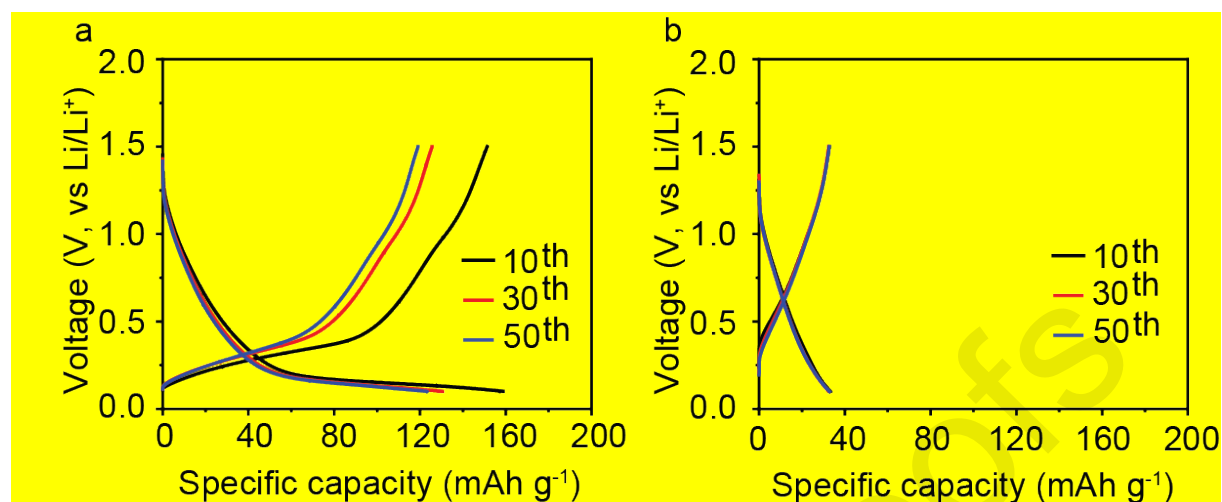


Fig. S1. The comparison of 10th, 30th and 50th charging and discharging cycles between (a). L-PPH and (b). C-PPH electrodes. The current density is 50 mA g⁻¹.

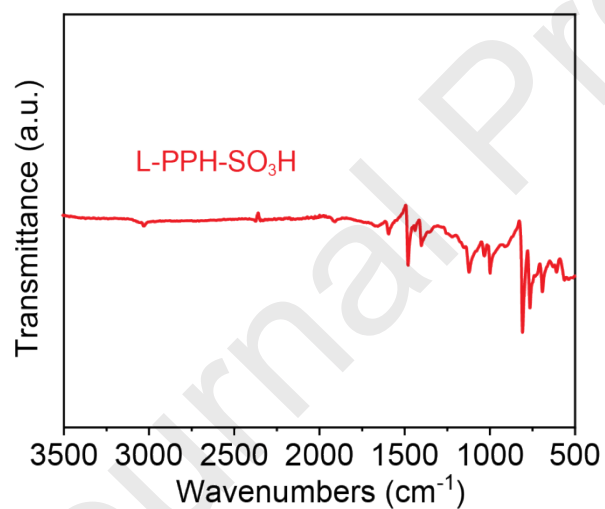


Fig. S2. Infrared spectroscopy of L-PPH-SO₃H.

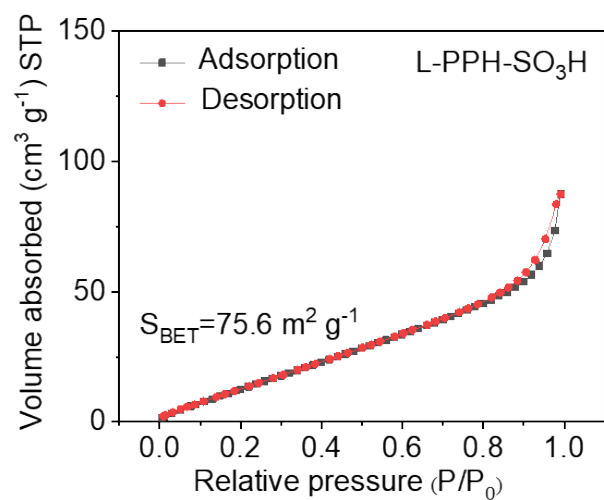


Fig. S3. The N₂ physisorption of L-PPH-SO₃H.

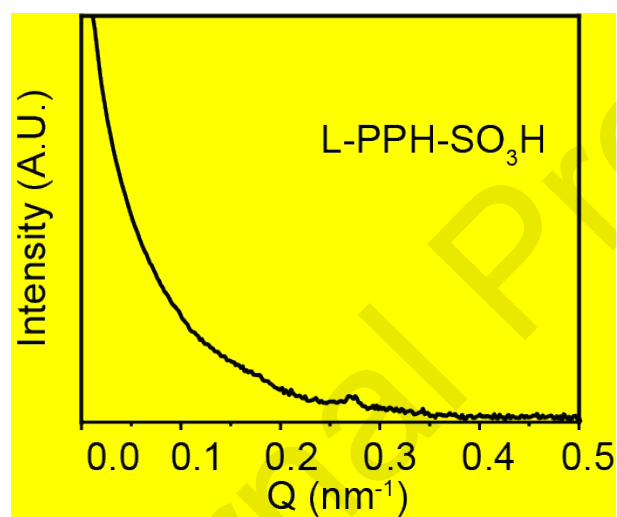


Fig. S4. SAXS curve of L-PPH-SO₃H.

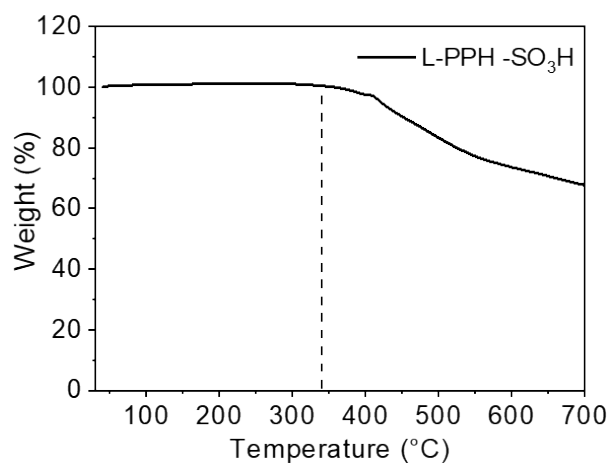


Fig. S5. Thermal gravimetric analysis of L-PPH-SO₃H material. The dash line indicates the starting temperature of decomposition.

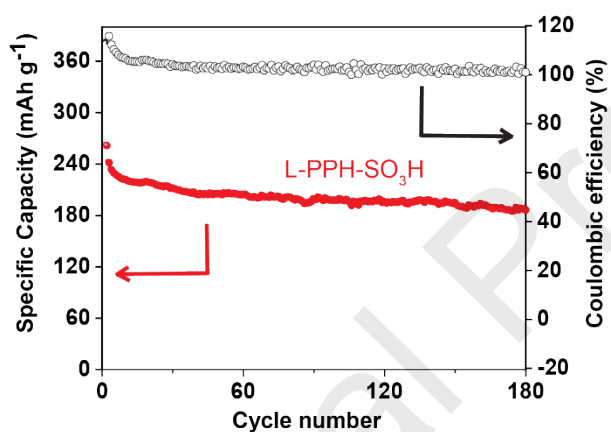


Fig. S6. The long cycle performance of L-PPH-SO₃H under a current density of 50 mAh g⁻¹ for 180 cycles.

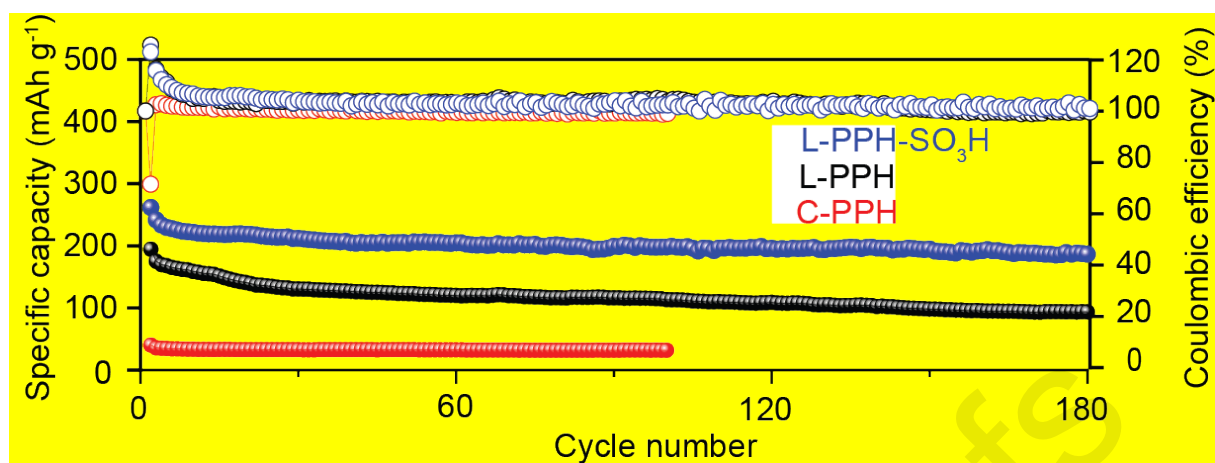


Fig. S7. The comparison of long-term cycling performance between L-PPH, C-PPH and L-PPH-SO₃H under current density of 50 mA g⁻¹.

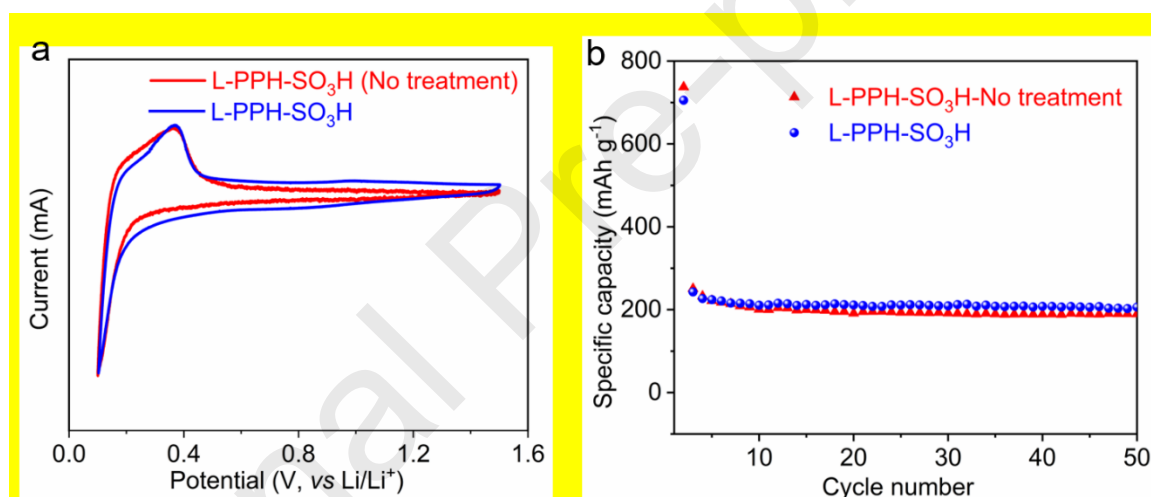


Fig. S8. (a). CV curves of the cell with L-PPH-SO₃H and L-PPH-SO₃H without H₂O₂/HCl treatment process (abbreviated as L-PPH-SO₃H-No treatment), (b). Cycling performance of cells at same current density of 50 mA g⁻¹ between L-PPH-SO₃H and L-PPH-SO₃H-No treatment.

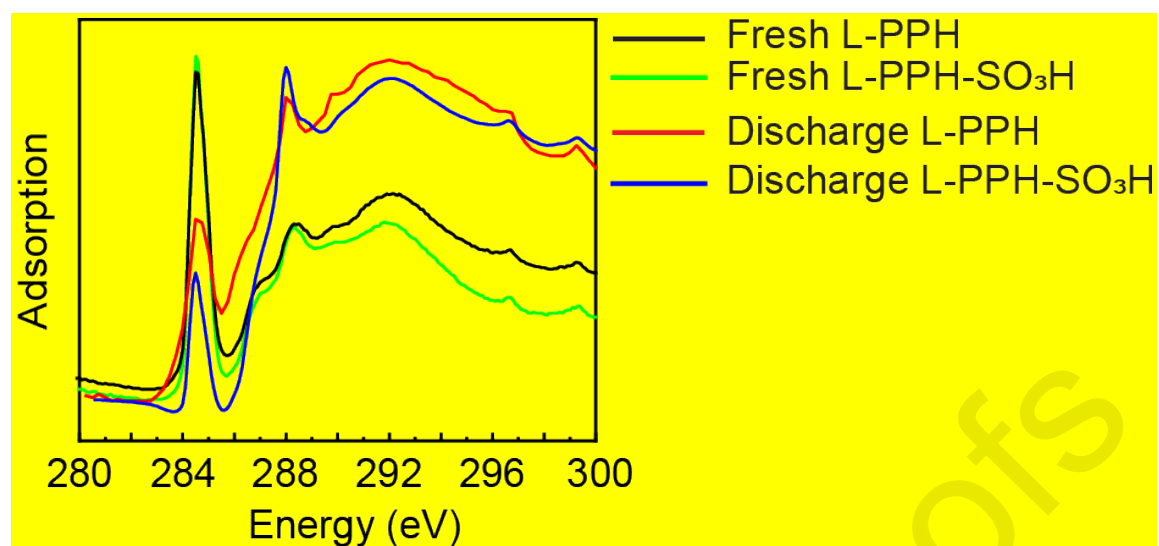


Fig. S9. A Comparison of C k edge NEXAFS for L-PPH and L-PPH-SO₃H at fresh and discharge states.

2. Calculation of PPH Theoretical Storage Capacity

2.1 Theoretical storage capacity of L-PPH and C-PPH

The molecular weight of L-PPH is 74 g mol^{-1} . At a 1:1 ratio, the theoretical storage capacity of L-PPH can be calculated *via*

$Q_{\text{theoretical}} = (nF)/(3600 \cdot W) \text{ mAh g}^{-1}$, where n is the number of charge carrier, F is the faraday constant and W is the weight of the PPH-SO₃H anode.

Thus, the $nF/W = 1 \cdot 6.02 \cdot 10^{23} \text{ mol}^{-1} \cdot 1.602 \cdot 10^{-19} \text{ C} / 74 \text{ g mol}^{-1} = 1303.2 \text{ C g}^{-1}$, so the $Q_{\text{theoretical}} = 1303.2 / 3600 \cdot 1000 = 362 \text{ mAh g}^{-1}$, the measured capacity of L-PPH is 194 mAh g^{-1} , corresponding to 0.54 Li^+ per C_6 .

Similarly, the molecular weight of C-PPH is 75.5 g mol^{-1} . Therefore, the theoretical storage capacity of C-PPH is:

$Q_{\text{theoretical}} = 1 \cdot 6.02 \cdot 10^{23} \text{ mol}^{-1} \cdot 1.602 \cdot 10^{-19} \text{ C} / 75.5 \text{ g mol}^{-1} = 1277.4 \text{ C g}^{-1}$, so the $Q_{\text{theoretical}} = 1277.4 / 3600 \cdot 1000 = 355 \text{ mAh g}^{-1}$, the measured capacity of L-PPH is 39 mAh g^{-1} , corresponding to 0.11 Li^+ per C_6 .